

# Microsphere kinematics from the polarization of tightly focused nonseparable light

Stefan Berg-Johansen,<sup>1,2</sup> Martin Neugebauer,<sup>1,2</sup> Andrea Aiello,<sup>1</sup>  
Gerd Leuchs,<sup>1,2</sup> Peter Banzer,<sup>1,2,3</sup> and Christoph Marquardt<sup>1,2,\*</sup>

<sup>1</sup>*Max Planck Institute for the Science of Light, Staudtstr. 2, D-91058 Erlangen, Germany*

<sup>2</sup>*Institute of Optics, Information and Photonics,*

*University Erlangen-Nuremberg, Staudtstr. 7/B2, D-91058 Erlangen, Germany*

<sup>3</sup>*Institute of Physics, University of Graz, NAWI Graz, Universitätsplatz 5, 8010 Graz, Austria*

Recently, it was shown that vector beams can be utilized for fast kinematic sensing via measurements of their global polarization state [Optica **2**(10), 864 (2015)]. The method relies on correlations between the spatial and polarization degrees of freedom of the illuminating field which result from its nonseparable mode structure. Here, we extend the method to the nonparaxial regime. We study experimentally and theoretically the far-field polarization state generated by the scattering of a dielectric microsphere in a tightly focused vector beam as a function of the particle position. Using polarization measurements only, we demonstrate position sensing of a Mie particle in three dimensions. Our work extends the concept of back focal plane interferometry and highlights the potential of polarization analysis in optical tweezers employing structured light.

## I. INTRODUCTION

Optical beams with a nonseparable mode structure [1, 2] have recently garnered attention in a wide range of subfields in optics, including generalized optical coherence theory [3], simulations of quantum mechanical systems [4], quantum channel characterization and correction [5], diffraction-free beam propagation [6], broadband cavity design [7], and metrology [8]. In this context, vectorial structured light plays a major role [9]. The nonseparability occurring between polarization and spatial degrees of vector beams was recently utilized for fast kinematic sensing based on polarization measurements [10].

In the present work, we extend the idea of position sensing with nonseparable modes to the nonparaxial regime, relevant to optical tweezers [11, 12] and nano-optics [13, 14]. In this regime, Gauss's law  $\nabla \cdot \mathbf{E} = 0$  couples different polarization components of laterally bounded fields, leading to a complex polarization structure in the focal region even for fields which are homogeneously polarized in the paraxial approximation [15–19]. Both radially polarized beams [20–25] and polarization effects [26–29] have been studied in optical tweezers in the past, and existing approaches to 3D sensing include methods with multiple beams [30], imaging [31, 32], and digital holography [33]. Of particular interest for the present work is the concept of back focal plane interferometry [34–40], where a particle-position-dependent phase delay between incoming and scattered field, due to the Gouy phase, is exploited for axial position sensing. In this approach, the lateral position is detected with a quadrant diode. A theoretical analysis of optimal position measurements of a dipole in a strongly focused field with polarization-insensitive detectors was recently given in [41].

Here, instead of spatially partitioning the field with a quadrant diode, we consider a partition in polarization space. First, we investigate the polarization state of forward scattered light from dielectric microspheres in the focal region of a tightly focused radially polarized beam as a function of particle position. We find a strong correlation between particle position and far-field polarization state. Through numerical simulations, we show that the essential features of the observed polarization structure can be reproduced by an electric dipole model, and that a similar, albeit overall weaker, particle-position-dependent polarization structure arises also for a linearly polarized Gaussian beam, which has separable degrees of freedom in the paraxial approximation. We numerically compare the signals obtained from polarization measurements with those obtained from quadrant diode detection for the same system. Next, we demonstrate experimentally that three-dimensional position sensing of a particle moving in the focal region of a tightly focused radially polarized beam is feasible using polarization data only. Our results suggest that polarization analysis in optical tweezers, combined with structured input light, presents a promising complement to existing approaches.

## II. METHODS

### A. Theory

The main principle of the investigated scheme is described in Fig.1a. It is equivalent to the experimental setting. An incoming tightly focused beam of light — wave fronts marked as gray lines — interacts with a dielectric micron-sized particle (small gray circle). The local field distribution of the beam at the particle position excites a mode inside the particle, scattering light into the far-field. This scattered light (red phase fronts) interferes with the transmitted beam, changing the overall far-field intensity and polarization of the diverging beam,

\* Corresponding author: christoph.marquardt@mpl.mpg.de

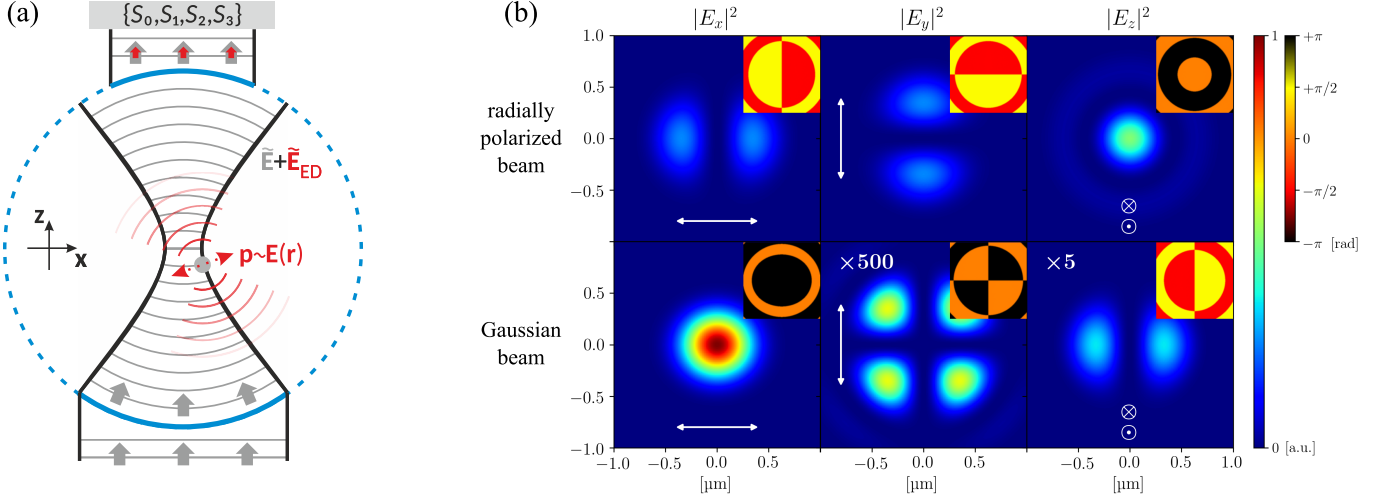


FIG. 1. (a) Experimental concept. A tightly focused beam excites a dielectric particle located in the focal region. The excited field is shown here as a linear electric dipole for simplicity, although for our beams it is in general a spinning dipole. The Stokes parameters of the electric field transmitted in the forward direction are measured as a function of the particle position. (b) Simulated electric energy density components in the focal plane of a tightly focused radially polarized beam (top) and an  $x$ -polarized Gaussian beam (bottom). The insets show the phase distribution for each component.

depending on the position of the particle relative to the focus. We partially collect this far field with a microscope objective and measure its Stokes parameters with a detection system. Since the position of the particle is encoded in the intensity and polarization state of the transmitted light, we can infer the position of the particle relative to the beam using the measured Stokes parameters.

For an exemplary theoretical description of our concept, we first consider the incoming tightly focused monochromatic beam of light. The vectorial angular spectrum (VAS) of the beam  $\tilde{\mathbf{E}}(k_x, k_y)$  — the VAS is defined with respect to the  $x$ - $y$ -plane (focal plane with  $z = 0$ ) — and the real space field distribution  $\mathbf{E}(\mathbf{r})$  with  $\mathbf{r} = (x, y, z)$ , are linked by a vectorial Fourier transformation,

$$\mathbf{E}(\mathbf{r}) = \iint dk_x dk_y \tilde{\mathbf{E}}(k_x, k_y) \exp(i\mathbf{k}\mathbf{r}). \quad (1)$$

All plane waves propagate in the positive  $z$ -direction ( $k_z > 0$ ). The theoretical electric field distribution in the focal plane for two beam types is shown in Fig. 1b. The real space field distribution determines the interaction with the particle. For the sake of simplicity, we only consider the fundamental electric dipolar mode of the dielectric particle, neglecting all magnetic and higher order electric resonances. The excited electric dipole moment is proportional to the local electric field,  $\mathbf{p}(\mathbf{r}_0) = \alpha_e \mathbf{E}(\mathbf{r}_0)$ , with  $\alpha_e$  being the electric polarizability of the particle and  $\mathbf{r}_0$  its position. The particle-position-dependent emission of the excited electric dipole moment in the VAS

representation reads [18]

$$\tilde{\mathbf{E}}_{ED}(k_x, k_y, \mathbf{r}_0) = [\mathbf{M}] \mathbf{E}(\mathbf{r}_0), \quad (2)$$

where

$$[\mathbf{M}] = \frac{i\alpha_e k^2 e^{i\mathbf{k}\mathbf{r}_0}}{8\pi\epsilon_0 k_z} \begin{pmatrix} 1 - \frac{k_x^2}{k_0^2} & -\frac{k_x k_y}{k_0^2} & -\frac{k_x k_z}{k_0^2} \\ -\frac{k_x k_y}{k_0^2} & 1 - \frac{k_y^2}{k_0^2} & -\frac{k_y k_z}{k_0^2} \\ -\frac{k_x k_z}{k_0^2} & -\frac{k_y k_z}{k_0^2} & 1 - \frac{k_z^2}{k_0^2} \end{pmatrix}.$$

The superposition of the VAS of the incoming beam with the VAS of the excited dipole moment results in the total VAS,

$$\tilde{\mathbf{E}}_T(k_x, k_y, \mathbf{r}_0) = \tilde{\mathbf{E}}_{ED}(k_x, k_y, \mathbf{r}_0) + \tilde{\mathbf{E}}(k_x, k_y). \quad (3)$$

As a next step, we take into account the detection geometry and calculate the total field distribution behind an aplanatic microscope objective with focal length  $f$  used for collecting the transmitted beam and the scattered light. The objective is confocally aligned with respect to the incoming tightly focused beam, implying that the field behind the objective is collimated (paraxial) with  $E_T^z \approx 0$  as long as the particle is close to the focal plane ( $z \ll f$ ). Using the formalism introduced in [15] to describe the rotation of the field vectors and the energy conservation at the reference sphere of the microscope objective, we arrive at the  $x$ - and  $y$ -components of the transmitted field,

$$\begin{pmatrix} E_x(k_x, k_y, \mathbf{r}_0) \\ E_y(k_x, k_y, \mathbf{r}_0) \end{pmatrix} \propto [\mathbf{R}] \tilde{\mathbf{E}}_T(k_x, k_y, \mathbf{r}_0), \quad (4)$$

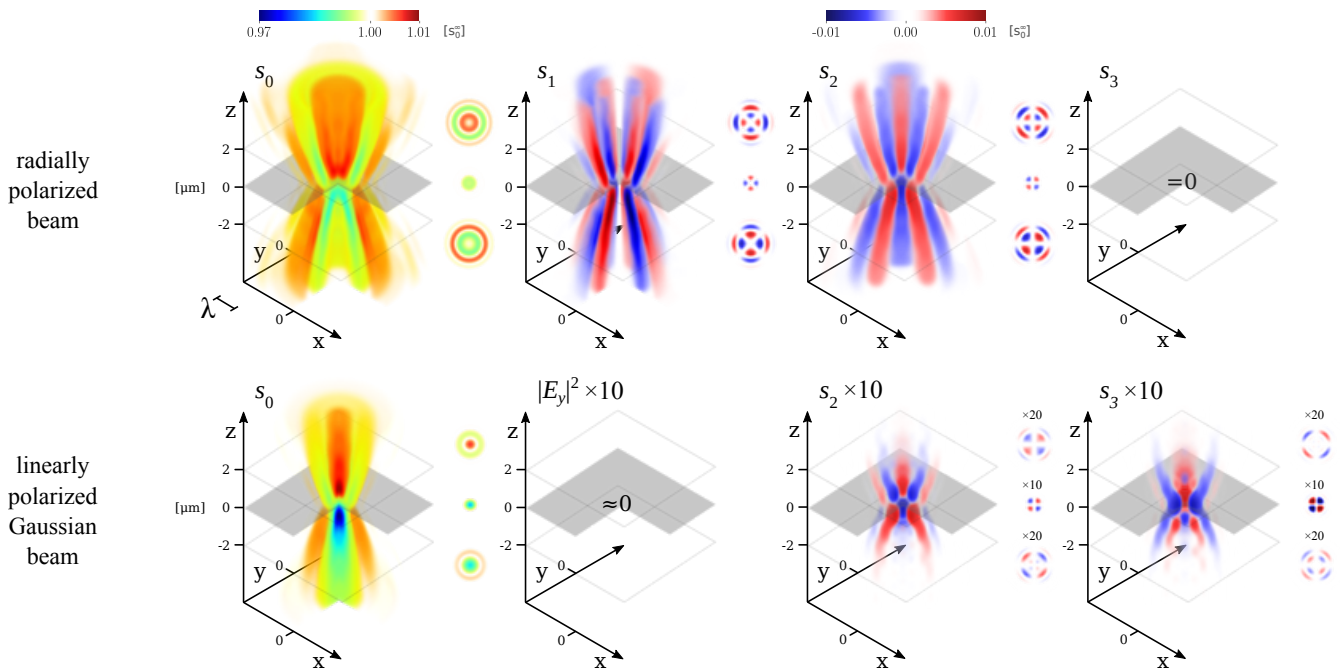


FIG. 2. Numerical simulation of the position-dependent global polarization state in the far-field for a  $\varnothing 2 \mu\text{m}$  ( $= 1.88 \lambda$ ,  $n = 2.6$ ) particle in the focal region of a radially polarized beam (top) and a linearly polarized Gaussian beam (bottom), with focusing NA 0.87.  $s_0$  (intensity) is normalised to the background value (without a particle), while  $s_1, s_2, s_3$  are normalised to the corresponding value of  $s_0$  at each coordinate. For the Gaussian beam, the  $y$ -polarized intensity component  $|E_y|^2$  is shown in place of  $s_1$ , as this Stokes parameter is dominated by the  $x$ -polarized input state. For clarity, background values are rendered transparently, and the front quadrant is cut out to reveal a cross-section of the axial values (missing values can be inferred from symmetry). Each panel spans a volume of  $6 \times 6 \times 10 \mu\text{m}^3$ . The focal plane at  $z = 0$  is indicated in grey. Insets to the right of each volume show transverse cross-sections at  $\{\pm 2; 0\} \mu\text{m}$ . Multiplicative numbers indicate gain applied for better visibility. See the text for discussion.

where

$$[\mathbf{R}] = \sqrt{\frac{k_z}{k}} \begin{pmatrix} \frac{k_x^2 k_z}{k_\perp^2 k} + \frac{k_y^2}{k_\perp^2} & \frac{k_x k_y}{k_\perp^2} \left( \frac{k_z}{k} - 1 \right) & -\frac{k_x}{k} \\ \frac{k_x k_y}{k_\perp^2} \left( \frac{k_z}{k} - 1 \right) & \frac{k_x^2}{k_\perp^2} + \frac{k_y^2 k_z}{k_\perp^2 k} & -\frac{k_y}{k} \end{pmatrix}.$$

Finally, we calculate the local Stokes parameters defined by:  $S_0 = |E_x|^2 + |E_y|^2$ ,  $S_1 = |E_x|^2 - |E_y|^2$ ,  $S_2 = 2 \text{Re } E_x E_y^*$  and  $S_3 = -2 \text{Im } E_x E_y^*$ . An integration over the full back focal plane of the collecting objective results in the particle-position-dependent global Stokes vector  $\mathbf{S}(\mathbf{r}_0)$ . Throughout this paper, we use a unitless convention whereby  $s_0(\mathbf{r}_0)$  represents the integrated intensity normalized to the background value (i.e. without a particle), while  $s_1, s_2, s_3(\mathbf{r}_0)$  are normalized to the local intensity. The position dependence of  $\mathbf{s}(\mathbf{r}_0)$  is one of the main results of the manuscript.

## B. Simulation

Based on the theoretical model described in the previous section, a numerical simulation of the far-field Stokes vector  $\mathbf{s}(\mathbf{r}_0)$  was carried out for both a radially polarized

beam and a linearly polarized Gaussian beam. Figure 2 shows the simulated position-dependent global polarization state in the far field, using physical parameters similar to those of our experiment. For both beams, the on-axis  $s_0$  values display a positive gradient as the particle moves through focus in the  $+z$ -direction. This is a known effect which can be intuitively understood by considering the Gouy phase shift incurred by the incoming field [34–40].<sup>1</sup> Depending on the axial particle position, the phase relation – in the far field – between incoming field and the dipole field leads to destructive or constructive interference. This axial intensity gradient is larger for the Gaussian beam for our choice of parameters. The same interferometric principle leads here to a transverse structure for the Stokes parameters  $s_1, s_2, s_3$ . In accordance with the behavior observed for  $s_0$ , these patterns are inverted as the particle passes through focus in the axial direction.

For a laterally displaced particle outside of the focal plane, a radially polarized beam leads to polarization sig-

<sup>1</sup> It should be noted that the NA of the detection path is smaller than the NA of the incoming path.

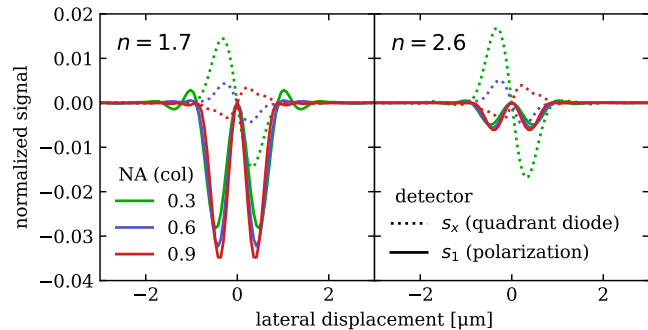


FIG. 3. Simulated response for the lateral displacement of a particle in the focal plane of a radially polarized beam for a quadrant diode measurement (dotted) and a polarization measurement (line), for selected particle refractive indices (left, right) and collection NAs (green, purple, red). The quadrant diode signal  $s_x$  represents the intensity difference between the right and left half-planes at the collection aperture. The remaining simulation parameters are chosen in accordance with the experiment (see Sec. II C).

nals which are an order of magnitude larger than the corresponding signals for a Gaussian beam. This example shows that the nonseparability of polarization and spatial degrees of freedom present in the initial paraxial beam affects the polarization distribution in the focal region, and that the resulting particle-position-dependent far-field polarization state can be tailored by suitable choice of paraxial input field and focusing NA.

In Figure 3, we compare the signal obtained from conventional quadrant diode detection with the signal obtained from polarization detection for the case of a laterally displaced particle in the focal plane of a tightly focused radially polarized beam. For quadrant detection, the magnitude and sign of the simulated signal are highly sensitive to the collection NA, in agreement with existing numerical and experimental results for Gaussian beams [35, 37]. The maximum gradient occurs on-axis, allowing for accurate measurement of small displacements about the origin. By contrast, the polarization signal has a vanishing gradient on-axis, and its maximum gradient occurs off-axis, close to the zero gradient of the quadrant signal. With the choice of parameters used here, the polarization measurement is also more sensitive to the particle's refractive index. These results suggest that the linear range of lateral displacement measurements can be enhanced by including the polarization degree of freedom. We note that quadrant- and polarization detection can, in principle, be performed simultaneously without optical losses.

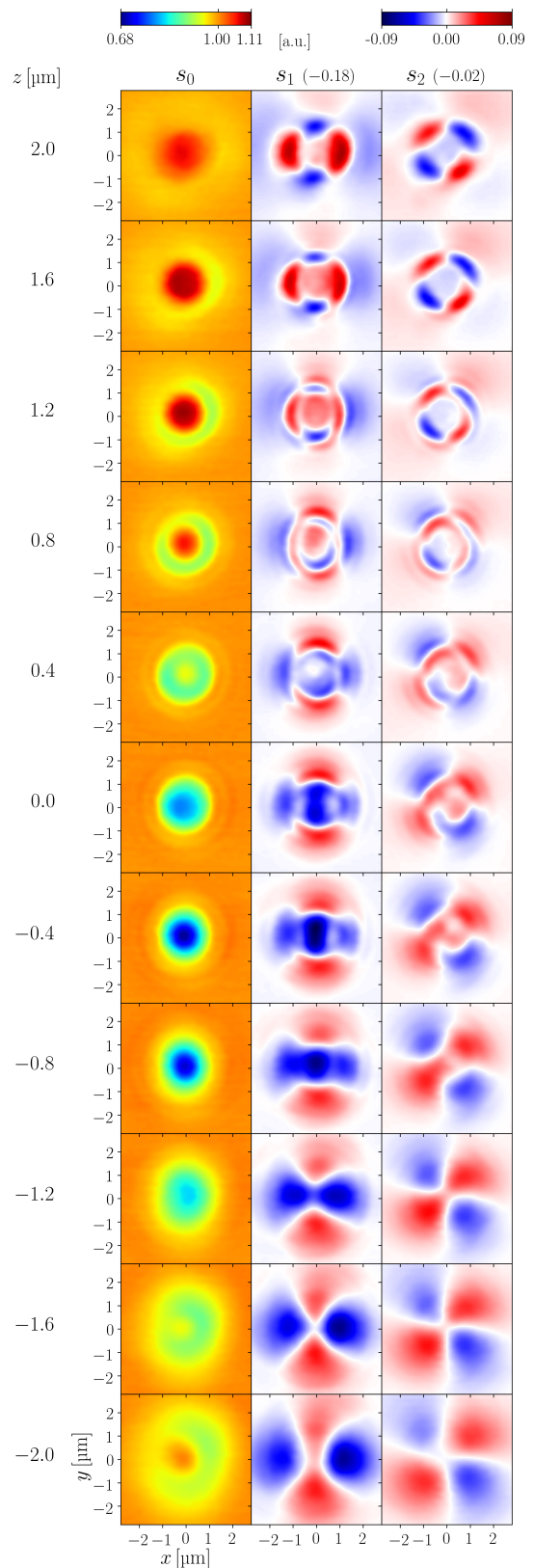


FIG. 4. Experimentally measured particle-position-dependent Stokes parameters  $\{s_0, s_1, s_2\}(\mathbf{r}_0)$  in the far field for a  $\varnothing 2 \mu\text{m}$   $\text{TiO}_2$  particle in TDE, in the focal region of a tightly focused radially polarized beam. See the text for details.

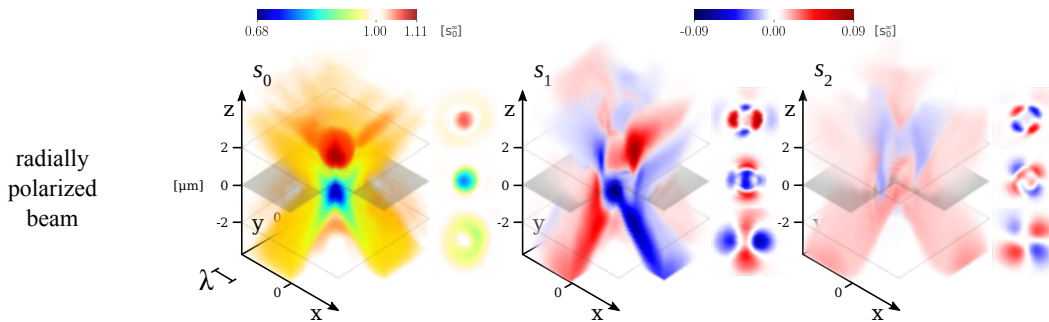


FIG. 5. Experimentally measured particle-position-dependent Stokes parameters  $\{s_0, s_1, s_2\}(\mathbf{r}_0)$  in the far field for a  $\varnothing 2 \mu\text{m}$   $\text{TiO}_2$  particle in TDE, in the focal region of a tightly focused radially polarized beam. As in Fig. 2, the front quadrant has been cut out for clarity. This makes  $s_1$  appear more intense than  $s_2$ , but as shown by the insets, the components are approximately balanced.

### C. Experiment

A cw laser centered at  $\lambda = 1064 \text{ nm}$ , emitting in a linearly polarized Gaussian mode, was passed through a liquid crystal mode converter followed by a Fourier filter to generate a radially polarized beam. The beam was focused with an aplanatic oil immersion objective (effective NA 0.9) onto single titania microspheres ( $\text{TiO}_2$ ,  $\varnothing 2 \mu\text{m}$ ,  $n \sim 2.5$ ) embedded in thio-diethanol (TDE,  $n_m = 1.50$ ) [42]. The transmitted light was collimated by a second objective and directed to a beam splitter cascade for the detection of the individual Stokes parameters.

For free particle measurements, a single particle was trapped in the beam. We used the piezoelectric motion stage on which the probe was mounted to nudge the particle in different directions out of the trap while recording the Stokes parameters  $\mathbf{s}(t)$ . Reconstructing the trajectory from polarization data requires the particle-position-dependent Stokes vector  $\mathbf{s}(\mathbf{r}_0)$ , which we measured experimentally. We temporarily increased the trap stiffness (via the laser power) and shifted the piezo stage in the  $+z$ -direction until the lower substrate made contact with the particle. This resulted in the particle becoming attached, and its position perfectly correlated with the subsequent motion of the piezo stage. The particle was scanned across a two-dimensional plane centered on the beam axis. By repetition, the particle-position-dependent Stokes vector  $\mathbf{s}(\mathbf{r}_0)$  was built up on a  $6 \times 6 \times 10 \mu\text{m}^3$  volume. The trajectory was reconstructed using an algorithm conceptually equivalent to [10]. Further details about the experimental setup and the tracking algorithm can be found in the Supplementary information below.

## III. EXPERIMENTAL RESULTS

### A. Particle-position-dependent Stokes parameters

Figure 4 shows the experimentally recorded particle-position-dependent Stokes parameters  $s_0, s_1, s_2$  for a  $2 \mu\text{m}$   $\text{TiO}_2$  particle scanned through a radially polarized beam. The beam's focal plane is approximately at  $z = 0$ , while  $z < 0$  and  $z > 0$  correspond to particle positions before and behind the focus, respectively, as in Fig. 2. Offsets (indicated in parentheses) were applied uniformly to  $s_1$  and  $s_2$  to make their background values zero for clarity of presentation. The full set of 40 planes (spaced by  $200 \text{ nm}$ ) is visualised in Fig. 5. The results reproduce the key features predicted by the simple theoretical model based on dipole scattering shown in Fig. 1a and Fig. 2, including the axial  $s_0$ -dependence, lateral dependence of  $s_1, s_2$ , and sign inversion relative to the focus.  $s_1$  and  $s_2$  are qualitatively identical up to a  $45^\circ$  rotation, as expected from the focal field distribution. When the particle is several Rayleigh ranges away from the focal plane, the parameters strongly resemble the polarization distribution of the paraxial mode, which agrees with intuition. Due to experimental imperfections, the measured  $s_3$  component (not shown) was not strictly zero everywhere. However, the nonzero pattern was reproduced identically between different scans and different particles, so that  $s_3$  was nevertheless included in the map  $\mathbf{s}(\mathbf{r}_0)$  used for position sensing.

### B. Position sensing

Figure 6 shows the results for position sensing of a free  $\text{TiO}_2$  particle placed in the focal region of a tightly focused radially polarized beam. In Panel 6a, the particle is at equilibrium in the optical trap potential behind the focal plane. In Panels 6b–e, the particle was nudged out of the trap by initiating a motion of the support-

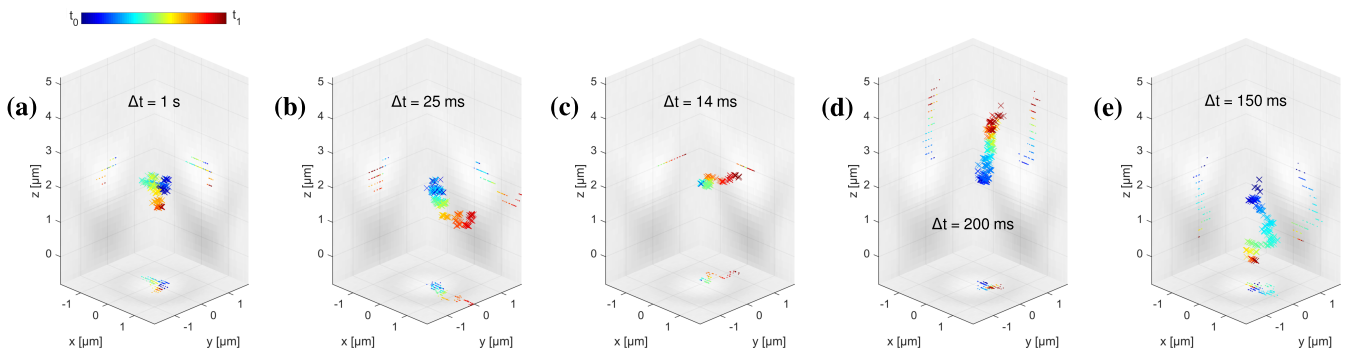


FIG. 6. Experimental results for three-dimensional position sensing of a  $\text{TiO}_2$  microsphere in the focal region of a tightly focused radially polarized beam. In Panel (a), the particle is undergoing Brownian motion in the trap potential, while in Panels (b)–(e) it is nudged in the  $+x$ -,  $+y$ -,  $+z$ -, and  $-z$ -directions, respectively. Motion is induced by moving the substrate supporting the medium in which the particle is suspended along the respective axes. Color indicates the time coordinate, normalized in each panel to match the duration of the measurement. The gray backdrops indicate the distribution of  $s_0(\mathbf{r}_0)$  in the plane through the origin, similar to Fig. 5 (brighter backdrop corresponds to higher values of  $s_0$ ).

ing piezo stage in the  $+x$ -,  $+y$ -,  $+z$ -, and  $-z$ -directions, respectively. The trajectory shown was inferred based on the measured polarization data only. Its direction was verified against the known motion of the piezo stage. For Panels b/c the motion was one order of magnitude faster than for Panels d/e, as shown by the indicated timescales. This demonstrates motion detection in three dimensions from polarization-resolved measurements of forward-scattered structured light.

Just like conventional quadrant diode measurements, sensing accuracy with this method is affected by pointing instabilities, which we minimized with large active photodiode areas ( $\varnothing$  500  $\mu\text{m}$ ). Remaining drifts on a timescale of minutes still caused a mismatch between  $\mathbf{s}(\mathbf{r}_0)$  and  $\mathbf{s}(t)$ . The results shown were enabled by observing the drift in the background value  $\mathbf{s}(\mathbf{r}_0 \rightarrow \infty)$  of each measurement and applying a suitable linear correction to each measured Stokes parameter  $s_i(t)$  in post-processing.

#### IV. CONCLUSION

We have investigated the far-field particle-position-dependent global polarization state resulting from a dielectric microsphere placed in a tightly focused vector beam. The observed polarization structure was explained in terms of a simple model which considers only the electric dipole contribution to the excited field. Our work thus extends the idea of back focal plane interferometry to the polarization degree of freedom. We have demonstrated three-dimensional position sensing from polarization measurements without spatially resolving the scattered field. Although all fields display some degree of polarization coupling when tightly focused, we have shown that paraxial vector beams lead to particularly large polarization gradients in the focal region compared to the more commonly used Gaussian beams, placing our work in the context of structured light with nonsepara-

ble degrees of freedom. Our numerical simulations indicate that polarization measurements, when combined with structured input light, can extend the transverse range of linearity of conventional quadrant diode detection schemes, and, depending on the system parameters, may even produce larger signal amplitudes. In addition, they are less sensitive to the collection NA than a quadrant detector. It is therefore conceivable that polarization analysis combined with structured input light could complement quadrant diode detection in optical tweezers. Measurements of this kind could, for example, be realized by placing a quadrant diode in each output port of a polarizing beam splitter, and considering the differences between the total intensities as well as the individual quadrant signals. The approach can be extended to vector beams with other polarization patterns, such as azimuthally polarized beams, “spiral” beams, their counter-rotating versions, and more exotic beams displaying nonzero net transverse angular momentum [43], as well as different wavelength regimes, opening many interesting avenues for exploration.

#### FUNDING INFORMATION

This project has partly received funding from the European Union’s Horizon 2020 research and innovation programme under the Future and Emerging Technologies Open grant agreement Superpixels No 829116.

#### ACKNOWLEDGMENTS

The authors thank Lucas Alber for suggesting thiodiethanol as mounting medium.

See the Supplementary information below for supporting content.

- [1] R. J. Spreuw, A classical analogy of entanglement, *Foundations of physics* **28**, 361 (1998).
- [2] A. Aiello, F. Töppel, C. Marquardt, E. Giacobino, and G. Leuchs, Quantum-like nonseparable structures in optical beams, *New Journal of Physics* **17**, 043024 (2015).
- [3] K. H. Kagalwala, G. Di Giuseppe, A. F. Abouraddy, and B. E. A. Saleh, Bell's measure in classical optical coherence, *Nature Photonics* **7**, 72 (2012).
- [4] A. N. de Oliveira, S. P. Walborn, and C. H. Monken, Implementing the Deutsch algorithm with polarization and transverse spatial modes, *Journal of Optics B: Quantum and Semiclassical Optics* **7**, 288 (2005).
- [5] B. Ndagano, B. Perez-Garcia, F. S. Roux, M. McLaren, C. Rosales-Guzman, Y. Zhang, O. Mouane, R. I. Hernandez-Aranda, T. Konrad, and A. Forbes, Characterizing quantum channels with non-separable states of classical light, *Nature Physics* 10.1038/nphys4003 (2017).
- [6] H. E. Kondakci and A. F. Abouraddy, Diffraction-free space-time light sheets, *Nature Photonics* **11**, 733 (2017).
- [7] S. Shabahang, H. E. Kondakci, M. L. Villinger, J. D. Perlstein, A. E. Halawany, and A. F. Abouraddy, Omniresonant optical micro-cavity, *Scientific Reports* **7**, 10336 (2017).
- [8] F. Töppel, A. Aiello, C. Marquardt, E. Giacobino, and G. Leuchs, Classical entanglement in polarization metrology, *New Journal of Physics* **16**, 073019 (2014).
- [9] H. Rubinsztein-Dunlop, A. Forbes, M. V. Berry, M. R. Dennis, D. L. Andrews, M. Mansuripur, C. Denz, C. Alpmann, P. Banzer, T. Bauer, E. Karimi, L. Marrucci, M. Padgett, M. Ritsch-Martel, N. M. Litchinitser, N. P. Bigelow, C. Rosales-Guzmán, A. Belmonte, J. P. Torres, T. W. Neely, M. Baker, R. Gordon, A. B. Stilgoe, J. Romero, A. G. White, R. Fickler, A. E. Willner, G. Xie, B. McMorran, and A. M. Weiner, Roadmap on structured light, *Journal of Optics* **19**, 013001 (2017).
- [10] S. Berg-Johansen, F. Töppel, B. Stiller, P. Banzer, M. Ornigotti, E. Giacobino, G. Leuchs, A. Aiello, and C. Marquardt, Classically entangled optical beams for high-speed kinematic sensing, *Optica* **2**, 864 (2015).
- [11] A. Ashkin, Acceleration and trapping of particles by radiation pressure, *Physical review letters* **24**, 156 (1970).
- [12] A. Ashkin, J. M. Dziedzic, J. E. Bjorkholm, and S. Chu, Observation of a single-beam gradient force optical trap for dielectric particles, *Optics letters* **11**, 288 (1986).
- [13] A. Bag, M. Neugebauer, P. Woźniak, G. Leuchs, and P. Banzer, Transverse Kerker Scattering for Angstrom Localization of Nanoparticles, *Physical Review Letters* **121**, 193902 (2018), arXiv: 1804.10176.
- [14] S. Nechayev, J. S. Eismann, M. Neugebauer, and P. Banzer, Shaping Field Gradients for Nanolocalization, *ACS Photonics* **7**, 581 (2020).
- [15] B. Richards and E. Wolf, Electromagnetic Diffraction in Optical Systems. II. Structure of the Image Field in an Aplanatic System, *Proceedings of the Royal Society of London. Series A, Mathematical and Physical Sciences* **253**, pp. 358 (1959).
- [16] W. L. Eriksson and S. Singh, Polarization properties of Maxwell-Gaussian laser beams, *Physical Review E* **49**, 5778 (1994).
- [17] R. Dorn, S. Quabis, and G. Leuchs, Sharper Focus for a Radially Polarized Light Beam, *Physical Review Letters* **91**, 10.1103/PhysRevLett.91.233901 (2003).
- [18] L. Novotny and B. Hecht, *Principles of Nano-Optics* (Cambridge University Press, 2012).
- [19] A. Aiello and M. Ornigotti, Near field of an oscillating electric dipole and cross-polarization of a collimated beam of light: Two sides of the same coin, *American Journal of Physics* **82**, 860 (2014).
- [20] S. Yan and B. Yao, Radiation forces of a highly focused radially polarized beam on spherical particles, *Physical Review A* **76**, 10.1103/PhysRevA.76.053836 (2007).
- [21] T. A. Nieminen, N. R. Heckenberg, and H. Rubinsztein-Dunlop, Forces in optical tweezers with radially and azimuthally polarized trapping beams, *Optics letters* **33**, 122 (2008).
- [22] M. Michihata, T. Hayashi, and Y. Takaya, Measurement of axial and transverse trapping stiffness of optical tweezers in air using a radially polarized beam, *Applied Optics* **48**, 6143 (2009).
- [23] Y. Kozawa and S. Sato, Optical trapping of micrometer-sized dielectric particles by cylindrical vector beams, *Optics Express* **18**, 10828 (2010).
- [24] M. G. Donato, S. Vasi, R. Sayed, P. H. Jones, F. Bonaccorso, a. C. Ferrari, P. G. Gucciardi, and O. M. Maragò, Optical trapping of nanotubes with cylindrical vector beams, *Optics Letters* **37**, 3381 (2012).
- [25] J.-B. Béguin, J. Laurat, X. Luan, A. P. Burgers, Z. Qin, and H. J. Kimble, Reduced volume and reflection for optical tweezers with radial Laguerre-Gauss beams, arXiv:2001.11498 [physics, physics:quant-ph] (2020), arXiv: 2001.11498.
- [26] K. Svoboda, C. F. Schmidt, B. J. Schnapp, and S. M. Block, Direct observation of kinesin stepping by optical trapping interferometry, *Nature* **365**, 721 (1993).
- [27] S. Bayouth, T. A. Nieminen, N. R. Heckenberg, and H. Rubinsztein-Dunlop, Orientation of biological cells using plane-polarized Gaussian beam optical tweezers, *Journal of Modern Optics* **50**, 1581 (2003), arXiv: physics/0308105.
- [28] R. S. Dutra, N. B. Viana, P. A. M. Neto, and H. M. Nussenzweig, Polarization effects in optical tweezers, *Journal of Optics A: Pure and Applied Optics* **9**, S221 (2007).
- [29] S. J. Parkin, R. Vogel, M. Persson, M. Funk, V. L. Loke, T. A. Nieminen, N. R. Heckenberg, and H. Rubinsztein-Dunlop, Highly birefringent vaterite microspheres: production, characterization and applications for optical micromanipulation, *Optics Express* **17**, 21944 (2009).
- [30] K. Visscher, S. P. Gross, and S. M. Block, Construction of multiple-beam optical traps with nanometer-resolution position sensing, *IEEE Journal of Selected Topics in Quantum Electronics* **2**, 1066 (1996).
- [31] T. Higuchi, Q. D. Pham, S. Hasegawa, and Y. Hayasaki, Three-dimensional positioning of optically trapped nanoparticles, *Applied optics* **50**, H183 (2011).
- [32] M. Yevnin, D. Kasimov, Y. Gluckman, Y. Ebenstein, and Y. Roichman, Independent and simultaneous three-dimensional optical trapping and imaging, *Biomedical Optics Express* **4**, 2087 (2013).
- [33] P. Memmolo, L. Miccio, M. Paturzo, G. D. Caprio, G. Coppola, P. A. Netti, and P. Ferraro, Recent advances in holographic 3d particle tracking, *Advances in*

- Optics and Photonics **7**, 713 (2015).
- [34] J. S. Batchelder and M. A. Taubenblatt, Interferometric detection of forward scattered light from small particles, *Applied Physics Letters* **55**, 215 (1989).
  - [35] A. Pralle, M. Prummer, E.-L. Florin, E. H. K. Stelzer, and J. K. H. Hörber, Three-dimensional high-resolution particle tracking for optical tweezers by forward scattered light, *Microscopy research and technique* **44**, 378 (1999).
  - [36] A. Rohrbach and E. H. K. Stelzer, Three-dimensional position detection of optically trapped dielectric particles, *Journal of Applied Physics* **91**, 5474 (2002).
  - [37] A. Rohrbach, H. Kress, and E. H. Stelzer, Three-dimensional tracking of small spheres in focused laser beams: influence of the detection angular aperture, *Optics Letters* **28**, 411 (2003).
  - [38] S. F. Tolić-Nørrelykke, E. Schäffer, J. Howard, F. S. Pavone, F. Jülicher, and H. Flyvbjerg, Calibration of optical tweezers with positional detection in the back focal plane, *Review of Scientific Instruments* **77**, 103101 (2006).
  - [39] J. Hwang and W. Moerner, Interferometry of a single nanoparticle using the Gouy phase of a focused laser beam, *Optics Communications* **280**, 487 (2007).
  - [40] L. Friedrich and A. Rohrbach, Tuning the detection sensitivity: a model for axial backfocal plane interferometric tracking, *Optics Letters* **37**, 2109 (2012).
  - [41] F. Tebbenjohanns, M. Frimmer, and L. Novotny, Optimal position detection of a dipolar scatterer in a focused field, *Physical Review A* **100**, 043821 (2019).
  - [42] T. Staudt, M. C. Lang, R. Medda, J. Engelhardt, and S. W. Hell, 2,2'-Thiodiethanol: A new water soluble mounting medium for high resolution optical microscopy, *Microscopy Research and Technique* **70**, 1 (2007).
  - [43] P. Banzer, M. Neugebauer, A. Aiello, C. Marquardt, N. Lindlein, T. Bauer, and G. Leuchs, The photonic wheel - demonstration of a state of light with purely transverse angular momentum, *Journal of the European Optical Society: Rapid Publications* **8**, 10.2971/jeos.2013.13032 (2013).
  - [44] R. Simon and N. Mukunda, Minimal three-component SU(2) gadget for polarization optics, *Physics Letters A* **143**, 165 (1990).



## Appendix: Supplementary information

An overview of our setup is shown in Fig. 7. The optical tweezer consisted of a pair of Leica 506195 HCX PL FLUOTAR 100x oil immersion objectives with NA 1.3. Samples were prepared by manually depositing a trace of silver conductive adhesive (SCA) on a BK7 glass substrate (thickness 80  $\mu\text{m}$ ,  $n = 1.51$ ). This highly reflective layer was helpful for calibrating the axial location of the focal plane as well as for focusing the white light image. A drop of particle solution was deposited near the dry SCA. Placeholders of the same thickness were placed laterally on the substrate followed by a second substrate on top (all BK7). Figure 8 shows the sample geometry to scale.

The entire sample configuration was placed on a piezo-controlled precision stage (PI PZ 82E) and brought into contact with the objectives via immersion oil (Leica Type F,  $n_e^{23} = 1.52$ ,  $v_e = 46$ ), index-matched to the BK7 substrate.

In order to minimize spherical aberrations, pure 2,2'-thiodiethanol (TDE,  $n_{\text{TDE}} = 1.50$ ) [42] was used as the mounting medium. TDE has an optical index very close to that of BK7 ( $n_{\text{BK7}} = 1.51$ ).

A pair of cold mirrors placed above and below the optical tweezer allowed white light from a halogen lamp (Fiberoptic-Heim Linos LQ 1100) to form an image of the particles on a CCD camera (ImagingSource DMK 31BU03 with objective). These mirrors were removed during polarization measurements in order to eliminate unnecessary polarization disturbances. Additionally, identical pairs of turning mirrors in a periscope configuration were used to walk the beam into and out of the optical tweezer without shifting the polarization state.

Back focal plane images of the upper objective were taken with an InGaAs camera above the optical tweezer (Xenics XS-450), by folding away a mirror. This enabled beam characterization, effective-NA estimation, and precise beam alignment.

Fig. 9 shows the detection of a Stokes parameter. Overall, three non-polarizing beam splitters were used to split the beam from the tweezer into sub-beams with relative fractions 22%, 18%, 19%, and 19% of the initial power. The beam splitters used for this purpose had uneven transmission and reflection coefficients for  $s$ - and  $p$ -polarisation, but were all aligned in the same plane. The mismatch of  $s$ - and  $p$ -transmission was corrected by a tilted glass plate in each sub-beam (labeled “F” in Fig. 9). The overall polarization transformation occurring between optical tweezer and Stokes parameter detection due to unspecified phase shifts was reverted in each sub-beam using a “polarization gadget” consisting of three wave plates [44]. The total transmission from tweezer to detectors was characterized for each sub-beam and factored into the responsivity of each detector. Large diodes ( $\varnothing \geq 500 \mu\text{m}$ ) were found to be helpful in minimizing drifts, as was enclosing the experiment against air convection.  $s_0$  was measured by direct detection while

$s_1, s_2, s_3$  were measured by direct difference photodetection. Each (difference) photocurrent was amplified by a transimpedance amplifying circuit inside each detector and recorded on an oscilloscope with 8 bit vertical resolution (LeCroy WaveSurfer 424).

Scanning measurements were performed by programming the piezo stage controller (PI E-710.3CD v7.040) to trace out a comb-like trajectory covering a rectangular area of the current transverse plane, as shown in Fig. 10. This was repeated in axial steps of 200 nm in order to cover the volume of interest. A single scan had a duration of 8.16 s, during which the Stokes parameters were measured continuously. After completion, the  $(x, y)$  coordinates were queried from the controller with a time resolution of 1 ms (Fig. 10). A regular grid was then constructed by linear tessellation inside the region of interest. The full map  $\mathbf{s}(\mathbf{r})$  was built up by repeating this process, typically over 50 planes.

From a measurement  $\mathbf{s}(t)$  of a free particle, the likelihood function

$$L(\mathbf{s}|\mathbf{r}, t) = \prod_{i=0}^3 \frac{1}{\sigma_i(2\pi)^{4/2}} \exp \left\{ -\frac{(s_i(t) - s_i(\mathbf{r}))^2}{2\sigma_i^2} \right\} \quad (\text{A.1})$$

was computed, where  $\sigma_i$  are the dark noise variances of the detectors, multiplied by a correction factor for tolerance of small experimental drifts. Using a constant prior distribution over a three-dimensional region

$$p(\mathbf{r}|t) = \sigma_{\text{prior}}^{-3} \prod_{k=\{x,y,z\}} \text{rect} \left( \frac{r'_k(t) - r_k(t_{-1})}{\sigma_{\text{prior}}} \right), \quad (\text{A.2})$$

where  $r_k(t_{-1})$  are the Cartesian components of the position inferred at the previous timestep, and  $\sigma_{\text{prior}}$  an empirically chosen width, we computed the posterior probability distribution  $P(\mathbf{r}|\mathbf{s}, t)$  via Bayes's theorem

$$P(\mathbf{r}|\mathbf{s}, t) = \mathcal{N} L(\mathbf{s}|\mathbf{r}, t) p(\mathbf{r}), \quad (\text{A.3})$$

with the normalization factor  $\mathcal{N} = [\int L(\mathbf{s}|\mathbf{r}, t) p(\mathbf{r}) d\mathbf{r}]^{-1}$ , denoting the probability of the probe being located at position  $\mathbf{r}$  conditional on having observed  $\mathbf{s}(t)$ . The maximum of this distribution was chosen as the new inferred position, and provided the center of the prior distribution for the next time step.

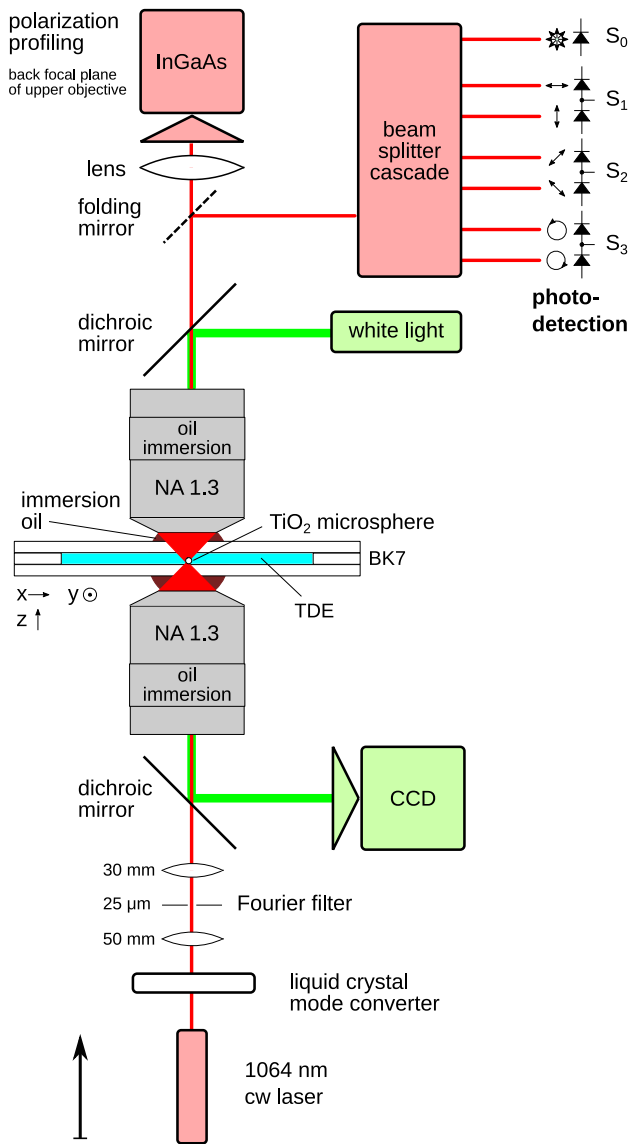


FIG. 7. Overview of experimental setup.

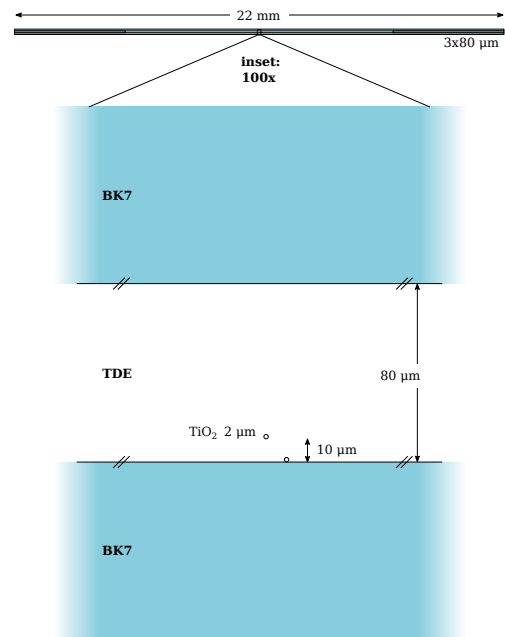
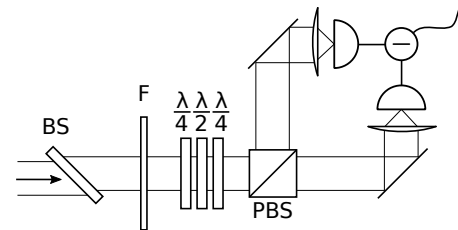
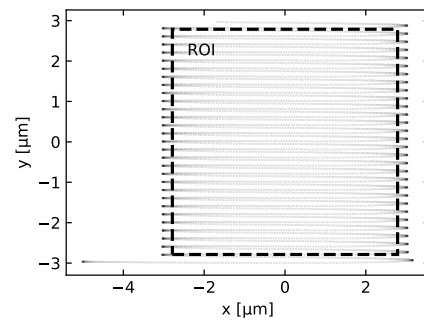


FIG. 8. Sample configuration (to scale).

FIG. 9. Detail of the detection setup for one of the  $s_{1,2,3}$  Stokes parameters. See text for description.FIG. 10. Typical report table from a scan mapping  $x$ - $y$ -position to time. The rectangle indicates the region of interest chosen for plotting.